Contents lists available at ScienceDirect

Materials Today Bio

journal homepage: www.journals.elsevier.com/materials-today-bio

Magnetic microspheres mimicking certain functions of macrophages: Towards precise antibacterial potency for bone defect healing

Qiao Zhou [a,b,c,1], Jun Liu [a,c,d,1], Jia Yan [a,b,c], Zhaobin Guo [e], Feimin Zhang [a,b,c,*]

[a] Jiangsu Key Laboratory of Oral Diseases, Nanjing Medical University, Nanjing, 210029, China
[b] Department of Prosthodontics, Affiliated Hospital of Stomatology, Nanjing Medical University, Nanjing, 210029, China
[c] Jiangsu Province Engineering Research Center of Stomatological Translational Medicine, Nanjing, 210029, China
[d] Nanjing Stomatological Hospital, Medical School of Nanjing University, Nanjing, 210008, China
[e] Institute for Nanobiotechnology, Johns Hopkins University, Baltimore, MD, 21218, USA

ABSTRACT

A variety of novel biomaterials have recently been developed to promote bone regeneration. However, the current biomaterials cannot accurately and effectively resist bacterial invasion. In this study, we constructed microspheres that mimic certain functions of macrophages as additives to bone repair materials, which can be manipulated as demanded to resist bacteria effectively and protect bone defect healing. Firstly, we prepared gelatin microspheres (GMSs) by an emulsion-crosslinking method, which were subsequently coated with polydopamine (PDA). Then, amino antibacterial nanoparticles obtained by a nanoprecipitation-self-assembly method and commercial amino magnetic nanoparticles were modified onto these PDA-coated GMSs to construct the functionalized microspheres (FMSs). The results showed that the FMSs possessed a rough topography and could be manipulated by a 100–400 mT static magnetic field to migrate directionally in unsolidified hydrogels. Moreover, *in vitro* experiments with near-infrared (NIR) showed that the FMSs had a sensitive and recyclable photothermal performance and could capture and kill *Porphyromonas gingivalis* by releasing reactive oxygen species. Finally, the FMSs were mixed with osteogenic hydrogel precursor, injected into the Sprague-Dawley *rat* periodontal bone defect of maxillary first molar (M1), and subsequently driven by magnetism to the cervical surface of M1 and the outer surface of the gel system for targeted sterilization under NIR, thus protecting the bone defect healing. In conclusion, the FMSs had excellent manipulation and antimicrobial performances. This provided us with a promising strategy to construct light-magnetism-responsive antibacterial materials to build a beneficial environment for bone defect healing.

1. Introduction

Bone defects in the oral and maxillofacial region impair patients' aesthetics and cause mastication and speech dysfunction [1]. Previous studies reported that implantation of specific material promoted bone regeneration [2,3]. However, due to the complex anatomy and being surrounded by various microbes, the wound surfaces in the oral and maxillofacial regions are more vulnerable to pathogenic microorganisms' infection [4–6]. Several strategies have been developed for anti-infection to ensure bone regeneration stability, including wound dressings (such as iodoform gauze and periodontal dressing paste) or antibiotics to reduce the occurrence of postoperative wound infection [7,8]. However, the anti-infection performance of these methods was limited. For example,

although the wound dressing can isolate the wound from the outside world, it provides a moist environment advantageous for bacteria growth, and some ingredients in the dressing would compromise wound healing [9]. For the use of antibiotics, the systemic administration of antibiotics decreases the accumulation of drugs in the wound sites, while the local administration has diffusion losses. This increased the possibility of drug resistance [10]. Therefore, it was necessary to develop an accurate and effective antibacterial strategy to prevent bone defects from bacterial attacks.

The precise human immune system may give us a compelling clue for precise sterilization. Macrophages are essential to the body's innate immunity and are important in anti-infection and wound healing processes [11,12]. Macrophages can capture bacteria and kill pathogenic

---

microorganisms by releasing reactive oxygen species (ROS) under physiological conditions [13,14]. Inspired by this "capture-controllable release of ROS sterilization" process, we attempted to construct microspheres that mimic certain functions of macrophages as additives for bone repair materials. Studies have shown that the reactive catechol groups on the polydopamine (PDA) coating formed by the auto-polymerization of dopamine could capture bacteria [15,16]. In addition, recent studies reported that IR780 iodide (IR780) could generate single oxygen ($^1O_2$) after laser irradiation at 808 nm [17], which provided a convenient way to controllably release ROS for anti-infection. However, the high levels of ROS will result in cell senescence through oxidative stress, which would impair the regeneration of bone defects [18]. Therefore, the preconceived microspheres should not only be delivered precisely to the target area (such as the cervical surface of the tooth or outer surface of implanted materials) to kill specific pathogens but also be kept away from the center of bone regeneration to decrease the influences of ROS on bone repair. The directional movement of magnetic microspheres under magnetic control may address this unmet need [19]. The functions of the microspheres partially mimic the natural macrophages, such as chemotaxis. Therefore, we hypothesize that by combining the above three elements (IR780, PDA, and magnetic microspheres) within a particle at several tens of microns in an ordered manner, it is possible to obtain the microspheres with "chemo-taxis-capture-sterilization" functionalities, which mimic the certain functions of natural macrophage and may achieve the requirement for precise sterilization.

In this study, we constructed such functionalized microsphere (FMS) through the ordered assembly of gelatin microsphere (GMS), PDA layer, IR780 loaded amino antibacterial nanoparticles (ANPs), and amino magnetic nanoparticles (MNPs). We also further tested it in multi-aspects, including morphology, physical and chemical properties, manipulation performances, antibacterial properties *in vitro* and *in vivo*, and its effects on bone defect healing.

2. Materials and methods

2.1. Materials and devices

Gelatin from porcine skin (type A, 300 g Bloom; Sigma-Aldrich, USA), span 80 ($C_{24}H_{44}O_6$; Sigma-Aldrich, USA), liquid paraffin ($C_{25}H_{43}NO_3$; Aladdin, China), 1,2-distearoyl-sn-glycero-3-phosphoethanolamine-N-[amino(polyethylene glycol)-5000] (DSPE-PEG5000-NH$_2$; 5000 Da; Sigma-Aldrich, USA), lecithin ($C_{42}H_{80}NO_8P$; Aladdin, China), lauric acid (LA; $CH_3(CH_2)_{10}COOH$; Aladdin, China), stearic acid (SA; $CH_3(CH_2)_{16}COOH$; Sigma-Aldrich, USA), glutaraldehyde aqueous solution (2.5% *wt/wt*; Leagene Biotechnology, China), acetone (Sinopharm Chemical Reagent, China), tris(hydroxymethyl)aminomethane hydrochloride (Tris-HCl; 1 mol L^{-1}, pH = 8.5; Leagene Biotechnology, China), dopamine hydrochloride ($(HO)_2C_6H_3CH_2CH_2NH_2 \cdot HCl$; Sigma-Aldrich, USA), 4 mg mL^{-1} amino MNPs (APTS@Fe$_2$O$_3$; Nanoeast, China), IR780 ($C_{36}H_{44}ClIN_2$; Sigma-Aldrich, USA), DMF (dimethylformamide; Sinopharm Chemical Reagent, China), 0.2 μm surfactant-free cellulose acetate membrane (Sartorius, Germany), centrifugal concentrator (Vivaspin 6; MWCO = 10 kDa; Sartorius, Germany), phosphotungstate negative staining buffer (2% *wt/wt*, pH = 7.0; Leagene Biotechnology, China), methacrylate gelatin (GelMA; type B; 300 g Bloom; degree of amino substitution is 60%; EFL-technology, China), bone morphogenetic protein-2 (BMP-2; 26 kDa; MedChemExpress, USA), chlorhematin (Aladdin, China), sterile defibrinated sheep blood (Nanjing Bianzhen Biotechnology, China), agar ($(C_{12}H_{18}O_9)_n$; biosharp, China), brain heart infusion (BHI; Oxoid, UK), *Porphyromonas gingivalis* W83 (*P. gingivalis* W83; Shanghai Bioresource Collection Center, China), phosphate buffered solution (PBS; HyClone, USA), live & dead bacterial staining kit (YEASEN, China), Masson's trichrome staining kit (Servicebio, China), hematoxylin-eosin (HE) staining kit (Servicebio, China), laser particle size analyzer (Zetasizer Nano ZS90; Malvern Panalytical, UK), pH meter

(FiveEasy Plus; Mettler Toledo, Switzerland), freezing dryer (FreeZone 4.5 L; Labconco, USA), X-ray photoelectron spectroscopy (XPS; Escalab 250Xi, Thermo Scientific, USA), magnetic property measurement system (MPMS-3; Quantum Design, USA), multi-mode microplate reader (SpectraMax M2e; MD, Germany), scanning electron microscope (SEM; JSM-7900F; JEOL, Japan), transmission electron microscope (TEM; JEM-1400Flash; JEOL, Japan), teslameter (TD8620; Tunkia, China), near-infrared (NIR) laser (VCL-808 nm M1-7 W; Beijing Honglan Optoelectronics Technology, China), thermograph (H21Pro; HIKMICRO, China), automatic colony counter (Scan1200; Interscience, France), inverted phase contrast microscope (DMILLED; Leica, Germany), inverted fluorescence microscope (DMI3000B; Leica, Germany), anaerobic & micro-aerophilic workstation (Bugbox M; BAKER, UK), electron paramagnetic resonance (EPR) spectrometer (EMXplus; Bruker, Germany), ultraviolet (UV) lamp (3 W, 405 nm; EFL-technology, China), oral surgery motor (Bien Air, Switzerland), micro-computed tomography (CT) (vivaCT80; SCANCO, Switzerland), upright microscope (DM4000 B; Leica, Germany).

2.2. Preparation of GMS and PDA modification

GMSs were prepared by the emulsion-crosslinking method, and the steps were as follows. 10% *wt/wt* aqueous gelatin solution was prepared as the water phase, and 1.5% *v/v* span 80 solution in liquid paraffin was prepared as the oil phase. After adding 30 mL oil phase to a 100 mL beaker and stirring at 60 °C, we added 6 mL preheated water phase and stirred at 400 rpm for 20 min. Then, the beaker was immediately put into an ice-water bath to maintain the temperature at 0–10 °C. Next, we slowly added 5 mL of 2.5% *wt/wt* glutaraldehyde aqueous solution and stirred for 2 h, then added 50 mL acetone and stirred for 1 h. After the GMSs were collected by centrifugation, we washed them with acetone, then transferred them to a glass dish until the acetone was evaporated at room temperature. Finally, these microspheres were transferred to the oven at 60 °C to dry the GMSs thoroughly. The morphology was observed by phase contrast microscope and SEM, and the particle size was measured.

To prepare PDA-coated GMSs, 800 mg GMSs were added to 40 mL of dopamine solution (2 mg mL^{-1} in 1 mol L^{-1} Tris-HCl at pH = 8.5). After incubating in the shaker at 200 rpm and kept away from light overnight, these microspheres were dried and collected.

2.3. Preparation and characterization of amino ANPs

Amino ANPs were prepared by the nanoprecipitation-self-assembly method, which refers to a light-responsive drug release system from previous literature with some modifications [20]. The steps were as follows: 48 μL IR780 solution (2.5 mg mL^{-1} in DMF) was added to 600 μL of the phase change material (PCM) stock solution (mass ration of LA and SA was 4:1, 4 mg mL^{-1}, diluted in methanol) and mixed well, then the mixture was added dropwise to the 3 mL phospholipid solution (mass ration of lecithin and DSPE-PEG5000-NH$_2$ was 3:1, 1 mg mL^{-1}, and diluted in 4% *v/v* ethanol aqueous solution) at 55 °C with gentle stirring, and then vigorously vortexed for 2–3 min. Next, the glass bottle containing the mixed liquor was quickly placed into an ice-water bath to cool for 1–2 min and stirred for 2 h at room temperature. When the mixture reached room temperature, it was vortexed for 1–2 min, filtered with a 0.2 μm filter, and concentrated (MWCO = 10 kDa) at 3800 g. Finally, the ANPs were washed with double distilled H$_2$O (ddH$_2$O) and stored in the dark at room temperature for further use.

In order to study the drug-loading properties of the nanoparticles, we used a multi-mode microplate reader to detect their ultraviolet–visible (UV–Vis) absorption spectra, with nanoparticles without IR780 (i.e., empty vehicles) and free IR780 as controls.

We further detected the encapsulation efficiency (*EE*) and loading efficiency (*LE*) of IR780 in the nanoparticles. The steps are as follows: The mass of IR780 used to prepare ANPs was recorded as m_0, then the

prepared ANPs were freeze-dried in the dark, weighed, and recorded as m_{ANP}. Next, these ANPs were dissolved into a concentrated solution, whose volume was denoted as V_1. Then the concentrated solution was diluted n times to detect the optical density (OD) at the absorption peak by a multi-mode microplate reader. Next, the loaded concentration of IR780 was calculated by Equation (1) (the standard curve of IR780 is shown in Supplementary Information, Fig. S1) and denoted as c_1. Finally, the EE was calculated according to Equation (2), and LE was calculated according to Equation (3).

$$c_1 \left[\mu g \ mL^{-1} \right] = (OD + 0.0162) \ / \ 0.1057 \times n \tag{1}$$

$$EE \ [\%] = (V_1 \times c_1) \ / \ m_0 \times 100\% \tag{2}$$

$$LE \ [\%] = (V_1 \times c_1) \ / \ m_{ANP} \times 100\% \tag{3}$$

In addition, we observed the Tyndall phenomenon of nanoparticle dispersion. The microscopic morphology was also observed by TEM. The sample preparation steps of the TEM were as follows: a carbon support film on 200 copper mesh was placed on the ANPs nano-suspension to float for 3 min. Then, it was transferred onto phosphotungstate negative staining buffer (2% wt/wt) to float for 3 min. After natural drying at room temperature, it was ready for TEM observation. Meanwhile, we also use a laser particle size analyzer to detect its hydrated particle size at room temperature. Finally, we also tested its photothermal properties. An NIR laser (wavelength at 808 nm with a power of 0.5 W cm^{-2}) was used to irradiate IR780 (15 µg mL^{-1}), and the temperature was recorded.

2.4. Characterization of amino MNPs

A 10 µL of the nanoparticle (APTS@Fe$_2$O$_3$) dispersion was pipetted to the carbon support film and dried at room temperature overnight, and its morphology was observed under TEM. The hydrated particle size was determined using the laser particle size analyzer at room temperature. For the magnetic properties, the amino MNPs were accurately weighed after freeze-drying and were subsequently analyzed using a magnetic property measurement system (MPMS-3) to plot the hysteresis loop.

2.5. Acquisition of FMS

The amino MNP dispersion and amino ANP dispersion were diluted with ddH$_2$O to make the pH at 6.24 (the corresponding concentration of MNP was 0.4 mg mL^{-1}) and 6.26 (the corresponding concentration of IR780 in ANP was 75 µg mL^{-1}) respectively, therefore meeting the reaction condition for covalent bonding between quinone groups and amino groups (aqueous solutions with pH within 5.5–9.5) [21]. To obtain FMSs, 10 mL diluted amino MNP dispersion was applied to incubate 800 mg PDA-coated GMSs at 37 °C. The MNPs were refreshed every day until one week. Then 10 mL diluted ANP dispersion was used to incubate them at 37 °C for one week with ANPs refreshed daily. The zeta potential of FMS was detected before and after the modification with MNPs and ANPs. To evaluate the magnetic property, these FMSs were attracted with a permanent magnet and were freeze-dried, followed by detection with the MPMS-3 to plot the hysteresis loop. The phosphorus element (P2p) on the surface of FMSs was detected by XPS, and the morphology of FMSs was characterized by phase contrast microscopy and SEM.

2.6. The handling performances of FMS under magnetic field and NIR

The handling performance of FMS under magnetism was evaluated. 4 mg FMSs were mixed with 2.5 mL of unsolidified 10% wt/wt GelMA aqueous solution. Their capacity for directional movement was detected using a static magnetic field of 100–400 mT at 37 °C.

To clarify the photothermal performance of FMSs under NIR, several groups were divided: group 1 (G1), pure GMS; G2, PDA-coated GMS; G3, PDA-coated GMS + MNP; G4, PDA-coated GMS + ANP; G5, PDA-coated

GMS + MNP + ANP (i.e., FMS). 1.5 mg of dry microspheres were taken from each group, and 20 µL of normal saline was added to make the microspheres infiltrated with the liquid to mimic the humid environment in vivo. The NIR laser (wavelength of 808 nm, power of 0.5 W cm^{-2}) was used to irradiate these samples (60 s/cycle, for three consecutive cycles). Meanwhile, the temperature was monitored with a handheld thermometer. The thermographs were exported, temperature variation curves were plotted, and the heating rates in 10 s irradiation were calculated. Furthermore, to control the temperature of the FMSs, we performed the following experiments: The temperature of the FMSs was rapidly increased at a power of 0.5 W cm^{-2} in the beginning, and the temperature was slowly decreased by switching the power to 0.1 W cm^{-2} when it reached 45 °C. When the temperature dropped to 41 °C, the power was switched back to 0.5 W cm^{-2} to raise the temperature to 45 °C. The cycle was repeated and continued for 2 min.

The photodynamic performance of FMSs was also examined. FMSs (5 mg) were resuspended with 100 µL ddH$_2$O and 100 µL capture agent (0.1 mol L^{-1} 2,2,6,6-tetramethylpiperidine). After being mixed thoroughly, they were irradiated by the NIR with a wavelength of 808 nm. The NIR power was cyclic switched (0.5 W cm^{-2}, 0.1 W cm^{-2}) as described above to maintain the temperature at 41–45 °C for 5 min. The supernatant was aspirated by a capillary tube and then detected by an EPR spectrometer.

2.7. In vitro antibacterial properties of FMS

The culturing protocol of P. gingivalis W83 refers to previous literature [22,23], which is as follows: P. gingivalis W83 was resuscitated at room temperature and incubated on BHI solid medium (consisting of 2.5 g agar, 7.5 g BHI, 250 mL ddH$_2$O, 25 mL sheep blood, 2.5 mL 0.5 mg mL^{-1} chlorhematin), then placed in anaerobic & microaerophilic workstation (10% CO$_2$, 10% H$_2$, and 80% N$_2$) for culture. After 2–3 passages, the bacteria in the exponential stage were transferred to BHI liquid medium (consisting of 7.5 g BHI, 250 mL ddH$_2$O, 2.5 mL 0.5 mg mL^{-1} chlorhematin). After culturing for 48 h, the bacteria solution was centrifuged at 4000 rpm for 10 min at 4 °C and resuspended with 1 mL of PBS. Afterward, it was diluted with BHI liquid medium ($OD_{600} = 0.8$) for further use.

The 10 mg sterile FMSs were co-cultured with 200 µL bacteria solution for 24 h. Then they were fixed, dehydrated, and subjected to conductive coating. The distribution of bacteria on the surface of FMSs was observed by SEM. Moreover, the material-bacterial mixtures were irradiated with NIR at 808 nm. Finally, the laser power was switched by cycling as described above (0.5 W cm^{-2}, 0.1 W cm^{-2}) to maintain the temperature at 41–45 °C for 5 min. The NIR-irradiated material-bacterial mixtures were used for the follow-up experiment with normal saline, PDA-coated GMS, PDA-coated GMS + MNP, and PDA-coated GMS + ANP set as control.

For the live and dead bacteria staining, DMAO, EthD-III, and normal saline were mixed (1:2:8, v/v/v; the total volume is 1 µL), then added to 100 µL NIR-irradiated material-bacterial mixtures. After incubating in the dark for 15 min, the dead or live bacteria were observed and counted under an inverted fluorescence microscope. Meanwhile, another 100 µL NIR-irradiated material-bacterial mixtures were added onto the BHI solid medium and cultured for one week. Finally, the number of colony-forming units (CFU) was counted using an automatic colony analyzer.

### 2.8. The antibacterial application of FMS during bone defect healing

All the animal experiments agreed with the ethical guidelines approved by the Institutional Animal Care and Use Committee of Nanjing Medical University, China (approval number: IACUC-2211027). Sprague-Dawley (SD) rats (Nanjing medical university, China) weighing 300–400 g were used. Before the periodontal surgery, BMP-2 loaded GMSs (BGMSs) were prepared in advance with the following steps: after washed with PBS, 0.5 g (dry weight) GMSs were mixed with 1.63 mL 100 µg mL^{-1} BMP-2 aqueous solution. They were incubated for one week in

the dark to obtain the BGMSs. The GelMA containing BGMSs served as a simple representative injectable osteogenic hydrogel, which was short for Gel-BGMS. Then SD *rats* were randomly divided into three groups: 1, blank control (BC) group, in which no material was injected; 2, Gel-BGMS group, in which the GelMA containing BGMSs was injected (25 μL 8% GelMA + 0.23 mg BGMSs); 3, Gel-BGMS/FMS^M + group, in which the GelMA containing BGMSs and FMSs was injected (25 μL 8% GelMA + 0.23 mg BGMSs + 0.23 mg FMSs) followed by a static magnetic field (100–400 mT) was used to attract the FMSs. The SD *rat* periodontal bone defect model was established, which referred to a previously described procedure with some modifications [2]. Specifically, SD *rats* were anesthetized with a 2% (*wt/wt*) sterile pentobarbital sodium aqueous solution. After mucosa preparation and draping, a 3 × 3 mm mucoperiosteum was excised mesial to the maxillary first molar (M1). Subsequently, a 5 mm additional incision was made along the alveolar ridge to lift the mucoperiosteal flap. Then, a full thickness round bone defect was generated with a round bur (4 mm in diameter) with the irrigation of sterile normal saline. Furthermore, a smaller round bur with a diameter of 2.3 mm was used to remove the residual bone tissues on the mesial surface of M1. After sutured, materials were injected through the reserved soft tissue defect mesial to M1. A static magnetic field at 100–400 mT was applied to drive the FMSs to the mesial neck region of M1 and the outer surface of the gel system (the specific implementation step is to place a permanent magnet with a field intensity of 100–400 mT on the gingival sulcus and surgical wound for 15 s), followed by immediate curing with the UV lamp. After surgery, the mesial gingival sulcus of M1 and the wound surface were applied with *P. gingivalis* (1 × 10^9 CFU mL^{-1} × 40 μL) every day for a week and irradiated with 808 nm NIR at 1, 3, 5, and 7 days (5 min, 41–45 °C). After irradiation, the bacteria were absorbed by absorbent paper points for the live/dead bacterial staining and observed under the inverted fluorescence microscope. Three months post-surgery, all the SD *rats* were euthanized. The maxillae were excised and fixed with an aqueous paraformaldehyde solution (4% *wt/wt*). These samples were scanned by micro-CT (55 kVp, 72 μA), followed by three-dimensional (3D) reconstruction and quantitative analyses. After that, they were decalcified, dehydrated, embedded, cut into slices, and stained with an HE staining kit and Masson's trichrome staining kit for observation under an upright microscope.

2.9. Statistical analysis

All experiments were repeated at least three times independently, and data are presented as mean ± standard deviation. A two-tailed Student's *t*-test was used to compare two groups of data, and one-way analysis of variance (ANOVA) with the least-significant difference (LSD) test was used for three or more data groups. $P < 0.05$ means the difference is statistically significant.
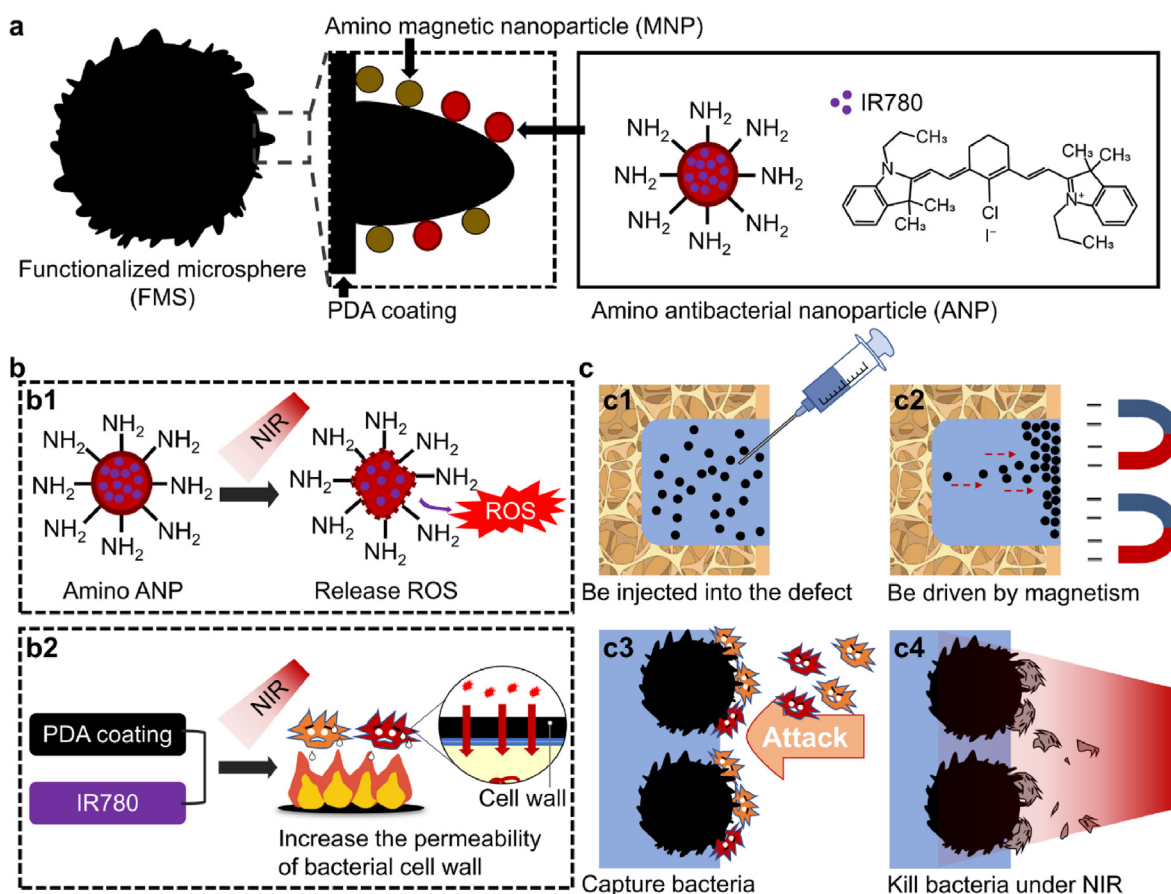
Fig. 1. Schematic diagram of FMS. (a) Structure. A rough PDA layer was wrapped on the surface of GMS, and amino MNPs and amino ANPs were further modified on the surface of the PDA layer to obtain FMS. The core of amino ANP is loaded with IR780. (b) The potential antibacterial mechanism. b1) Photodynamic effect. The inner core of amino ANP melted under the NIR, and IR780 was released to generate ROS; b2) Photothermal effect. The rise in temperature caused by the photothermal effect of PDA and IR780 under NIR will increase the permeability of bacterial cell walls and facilitate the entry of antibacterial substances into bacteria. (c) FMS had a "chemotaxis-capture-sterilization" function similar to natural macrophages. c1) FMSs were mixed with injectable hydrogel and injected into the bone defect, c2) then directionally moved to the target region driven by magnetism. c3) They trapped bacteria on their surfaces, c4) finally killed them under NIR, thus blocking the attack and protecting the wound.

3. Results and discussion

3.1. FMS design and conception

The schematic structure of the magnetic microsphere mimicking certain functions of macrophages constructed in this study is shown in Fig. 1a. GMSs native to macrophages in size were wrapped up with a rough PDA layer for trapping bacteria. The PDA coating was further modified with amino MNPs and amino ANPs. The core of the amino ANPs was loaded with IR780. The potential antibacterial mechanism of the FMS is shown in Fig. 1b: 1, photodynamic effect (the core of the ANPs melted under NIR, controllably released IR780, and generated ROS for sterilization); 2, photothermal effect (the rise in temperature caused by the photothermal effects of PDA coating and IR780 could increase the permeability of bacterial cell walls [24], promoting the entry of antibacterial substances into the bacteria).

This FMS possessed the capacity of "chemotactic-capture-kill," which was similar to that of natural macrophages (Fig. 1c). When FMSs were injected into the bone cavity loaded within an injectable hydrogel (Fig. 1c1), they could move to the target region under the control of magnetism (Fig. 1c2). They trapped bacteria on their surfaces (Fig. 1c3) and killed bacteria under NIR (Fig. 1c4), thus preventing bacterial attack.

3.2. Components of FMS

3.2.1. Construction of the base of FMS

We used PDA-coated GMS as the substrate for FMS. Firstly, GMSs were prepared successfully by an emulsion-crosslinking method. It was a pale-yellow powder with good flowability (Fig. 2a1). The microscope showed various microspheres with flat and smooth surfaces (Fig. 2a2-3). The particle size ranged between 5 and 70 μm (Fig. 2b). The average particle size was 33.76 ± 13.16 μm, which was close to the size of natural macrophages (21.2 ± 0.3 μm) [25].

To obtain the PDA-modified layer, we modified the surface of GMSs by the auto-polymerization of dopamine [26]. The modified GMSs were presented as a black powder from a macroscopical view. The microscope showed a rough surface modification layer (Fig. 2c), caused by the self-aggregation of dopamine in the solution to form some small PDA particles [27]. According to previous studies [21], the quinone groups of PDA coating could chemically react with the amino terminus to form covalent bonds in aqueous solutions at pH = 5.5–9.5 (Fig. 2d). Therefore, to construct FMS, we needed amino nanoparticles.

As the base of FMS, the PDA-coated GMS has the following effects: 1, In addition to the ability to further modify amino nanoparticles and capture bacteria mentioned above, the PDA coating also has a photothermal capacity [28,29]. 2, The PDA-coated GMS also provides a size
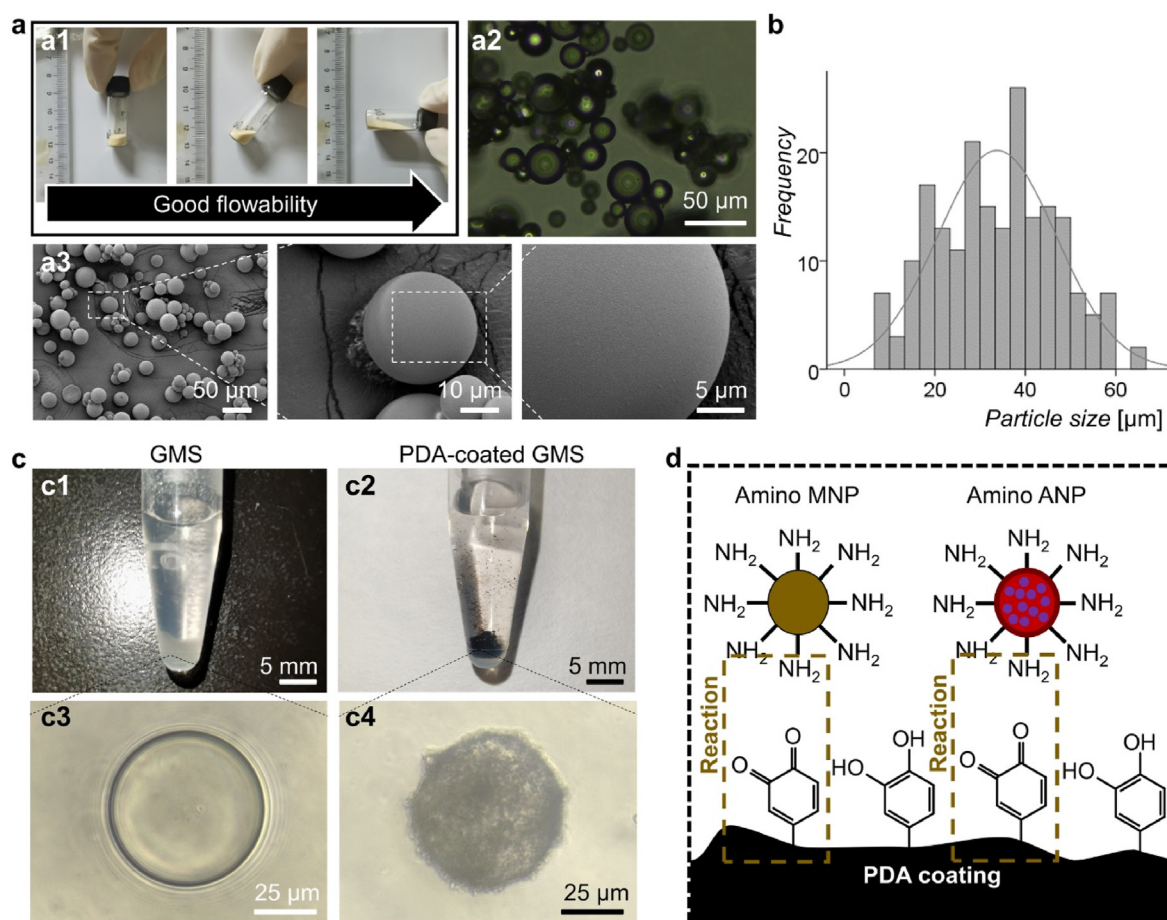
Fig. 2. The substrate of FMS (PDA-coated GMS). (a) Topography of GMS. a1) Macrophotograph. a2) Phase contrast microscope image. a3) SEM image. (b) Particle size distribution of GMSs. (c) Morphology of GMSs before and after PDA modification. c1-2) macroscopic photos; c3-4) phase contrast microscope photos. (d) The schematic shows that we can use the reaction of amino groups with quinone groups to covalently bind the two types of nanoparticles onto the surface of PDA-modified microspheres.

advantage. Modified onto the microspheres at several tens of microns, these nanoparticles can be fixed well at the desired position when used in combination with the injectable hydrogel, thus making the obtained hierarchical gel system stable. Without the microsphere, the use of nanoparticles alone may lead to the instability of the hierarchical structure due to the small size-mediated diffusion within the hydrogel system [30].

3.2.2. Amino ANP

The ANPs with a core-shell structure could be successfully prepared by the nanoprecipitation-self-assembly method, according to the previous study [20]. 1,2-distearoyl-sn-glycero-3-phosphoethanolamine-N-[methoxy(polyethylene glycol)-5000] (DSPE-PEG5000) was used to construct the shell of the nanoparticle [20]. The PEG5000 terminal of the molecule is exposed on the surface of the shell, contributing to stabilizing the nanoparticle dispersion system [31]. In this study, to obtain nanoparticles rich in amino groups on their surface, the DSPE-PEG5000 in the

material preparation process was replaced with DSPE-PEG5000-NH$_2$, which added an amino group to the end of PEG5000. This promoted the formation of amino groups layer on the surface of the particle shell (Fig. 3a1).

The core of the nanoparticles was a hydrophobic PCM composed of LA and SA (mass ratio = 4:1, referring to previous literature [20]), with a melting point of 40.09 °C (Supplementary Information, Fig. S2). It could controllably release the drug within the particle when melted. In this study, the drug contained in the hydrophobic core was IR780, a small molecule heptamethine indocyanine dye [32] that can heat up and produce ROS after NIR irradiation [17]. The detection with EPR further illustrated the ROS-releasing ability of this ANP (Supplementary Information, Fig. S3). The drug-loading properties of this ANP could be observed in the UV–Vis absorption spectra (Fig. 3a2). The result showed that a high absorption peak corresponding to free IR780 could be found in the spectrum of ANPs. Furthermore, this absorption peak was
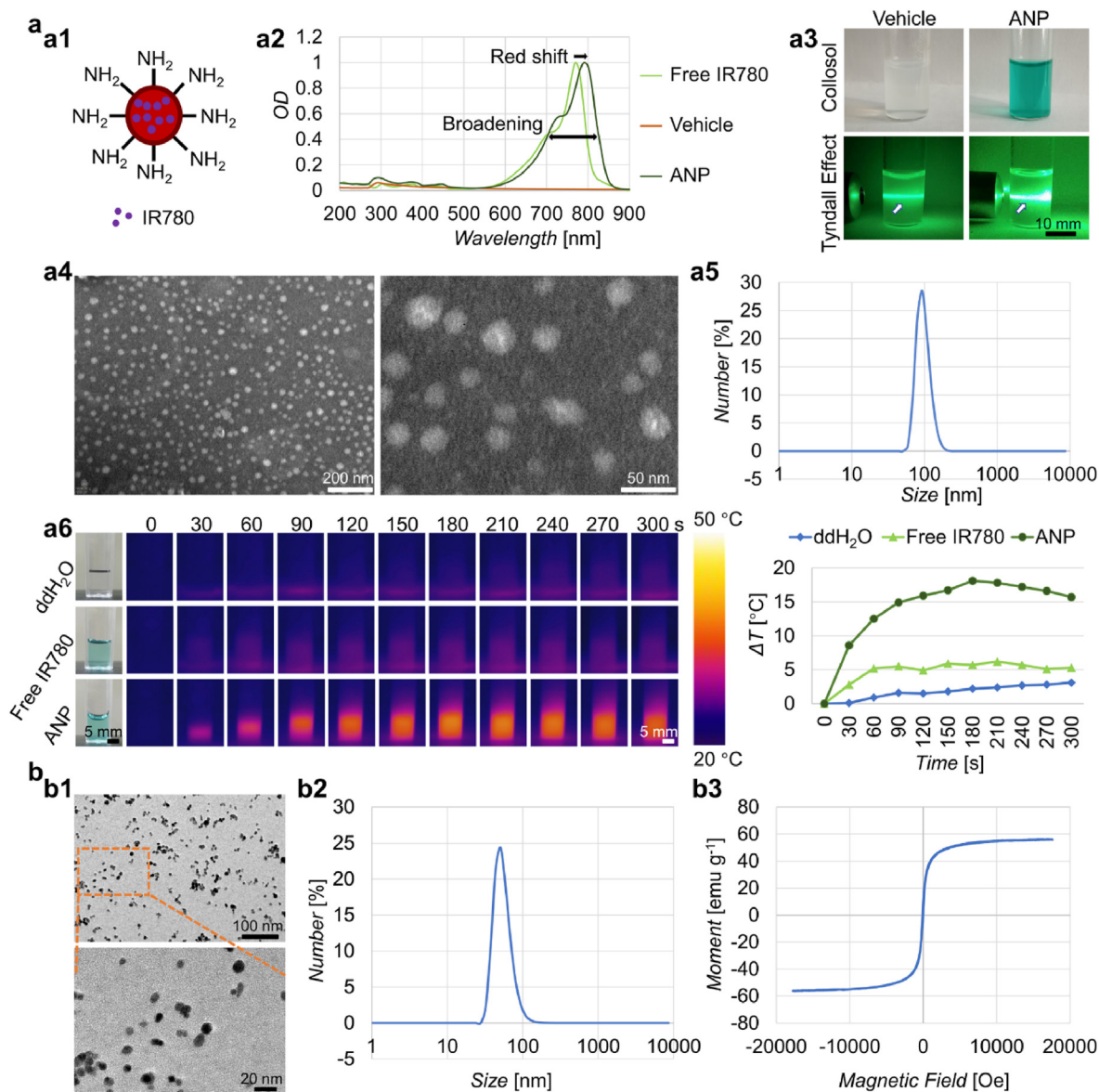
Fig. 3. Amino ANPs and MNPs. (a) Characterization of amino ANPs. a1) Schematic diagram of the structure. ANP consists of a shell with amino groups and a hydrophobic core loaded with IR780. a2) UV–Vis absorption spectra. The characteristic peak of ANPs is broadened and red-shifted compared to free IR780. a3) Macroscopic pictures of blank vehicles and ANPs dispersions, both with the Tyndall effect (the light path is indicated by the white arrow). a4) TEM image. a5) The hydrated particle size distribution. a6) Photothermal performance of ANPs under NIR. The left is the thermal image, and the right is the heating curve. (b) Characterization of amino MNPs. b1) TEM image. b2) Hydrate particle size distribution. b3) Hysteresis loop. (For interpretation of the references to colour in this figure legend, the reader is referred to the Web version of this article.)

broadened and red-shifted compared to the free IR780 (from 770 nm to 790 nm). This was caused by the hydrophobic interaction between IR780 and the PCM matrix [33,34], which indicated that IR780 has been successfully loaded into the hydrophobic core of the nanoparticles.

Moreover, we also noted that the *EE* and *LE* of IR780 in ANPs were 66.57 ± 0.86% and 3.56 ± 0.09%, respectively. The empty and the IR780-loaded vehicles possessed the Tyndall effect, indicating that the nanoparticles' dispersion system was a sol (Fig. 3a3). The TEM results showed the nanoparticle with a particle size of 10–50 nm (see Fig. 3a4) at an average particle size of 22.65 ± 5.68 nm. The hydrated particle size distribution is shown in Fig. 3a5, and the characteristic peak is located at 100.30 ± 7.65 nm.

The normal temperature of the human body is 36–37 °C, while the melting point of the nanoparticle core material was 40.09 °C. Therefore, it only needed to rise 3–4 °C to release the drug by melting the core. We detected the photothermal properties of the nanoparticles, and the results are shown in Fig. 3a6. Under NIR at a power density of 0.5 W cm^{-2}, the ANPs could rise more than 10 °C within 1 min, which reached the requirement that increased 3–4 °C mentioned above. Moreover, the ANPs possessed better photothermal properties than free IR780. It was attributed to the protection from the nanoparticle vehicle, which reduced the denaturation of IR780 under light [20]. In short, the ANP had a good photothermal effect, which would be beneficial to melting the core material to controllably release the contained drugs.

3.2.3. Amino MNPs

A commercial amino MNP was used in our study. The TEM results (Fig. 3b1) showed that the particle size ranged between 5 and 19 nm, and the average particle size was 10.08 ± 2.18 nm. Moreover, the hydrated particle size is shown in Fig. 3b2. The characteristic peak was located at 55.45 ± 0.62 nm. The hysteresis loop showed a saturation magnetization of 55 emu g^{-1} and the remanence and coercivity close to 0 (Fig. 3b3). This implied the superparamagnetic properties of the MNPs.

3.3. Acquisition of FMS

The FMS was obtained by modifying the two types of amino nanoparticles onto the PDA-coated GMS [21]. The surface charge of these microspheres before modification with MNPs and ANPs was −20.26 ± 0.85 mV, similar to the surface charge of PDA particles reported in previous studies [35]. Modification with MNP and ANP slightly decreased the negative charge of the microsphere surface to −18.49 ± 1.16 mV. We examined the modification effect of these nanoparticles on the FMS surface. We noted that the FMSs could be attracted by the permanent magnet (Fig. 4a1), and its saturation magnetization could reach 1.5 emu g^{-1} (Fig. 4a2), indicating that the MNPs have been successfully modified. Moreover, the remanence and coercivity were close to 0 and still possessed superparamagnetism. This reduces the influence of the magnetic field on the surrounding tissue when implanted into the body. The
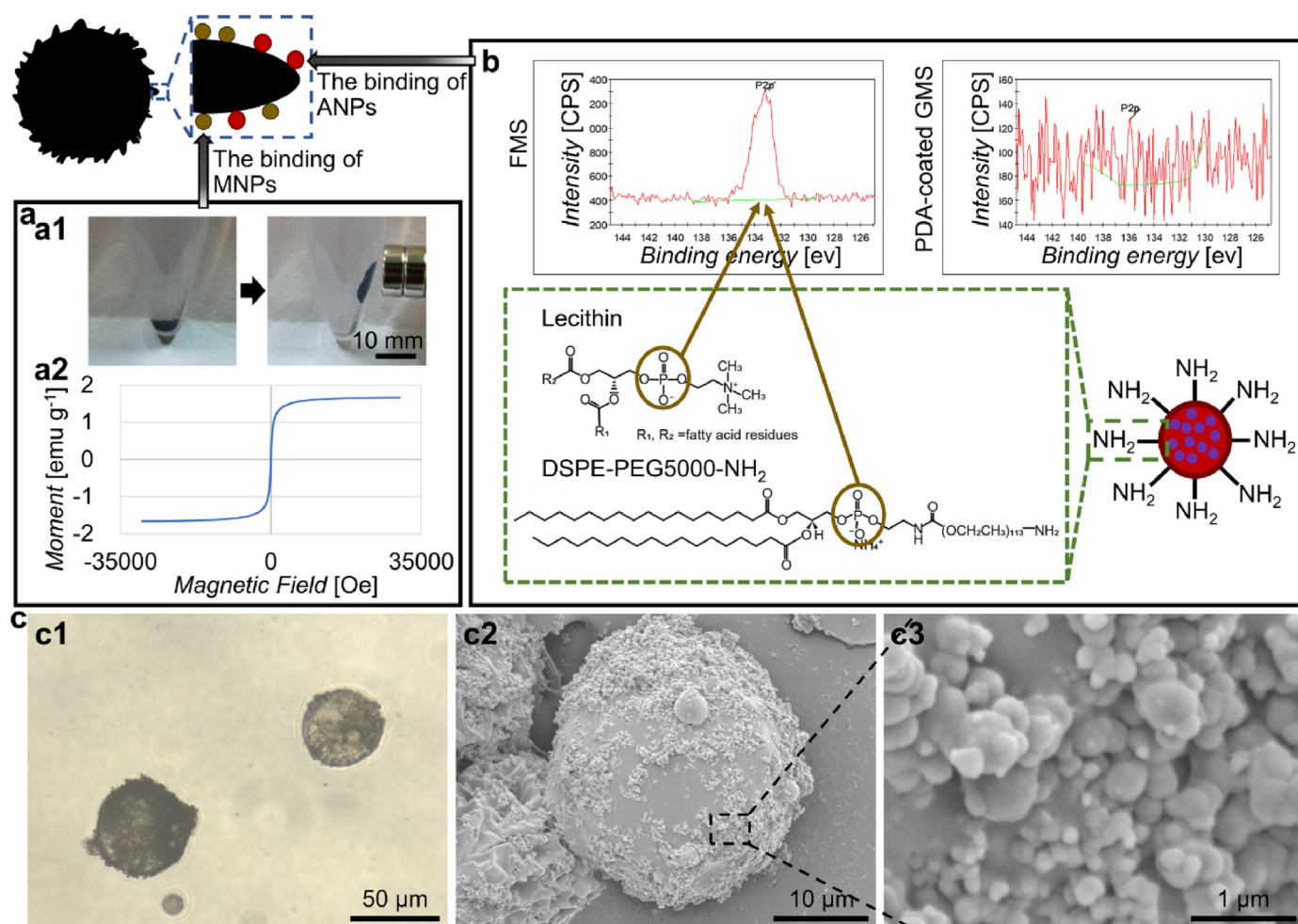
Fig. 4. Acquisition of FMSs. (a) Modification effect of MNP. a1) FMSs can be attracted by permanent magnets. a2) Magnetic hysteresis loop of FMSs; (b) Modification effect of ANP. The XPS result of FMSs showed a peak of phosphorus element, while the PDA-coated GMSs were without it. The peak of the phosphorus element corresponds to the shell component of the ANP (lecithin and DSPE-PEG5000-NH$_2$), indicating that the ANPs have been successfully modified onto the PDA coating. (c) Morphology of FMSs. c1) Phase contrast microscope image. c2-3) SEM image.

results of XPS are shown in Fig. 4b: contrasted to PDA-coated GMSs, a peak of phosphorus element could be detected on the surface of FMSs, which corresponded to the phosphorus element in the shell components (lecithin and DSPE-PEG5000-NH$_2$) of ANP, indicating that ANPs had also been successfully modified. These results indicated that both MNPs and ANPs were successfully modified onto the PDA-coated GMS. Therefore, we constructed the FMS successfully. In fact, besides this surface modification strategy for obtaining the magnetic microspheres, the one-spot loading strategy with high efficiency can also be adopted to obtain them [36]. In this study, we required an intermediate product (the pure GMSs) for later use in loading BMP-2, thus not adopting the one-spot loading strategy.

The phase contrast microscope and SEM results showed that the FMS had a rough surface (Fig. 4c), which would benefit the capture and killing

of bacteria [37,38]. Interestingly, the morphology of FMSs resembled native macrophages, which also possess a rough surface and villi-like structure [39].

3.4. Application performance of FMS in vitro

3.4.1. Manipulating FMS by magnetism and NIR

FMSs were mixed with unsolidified GelMA (an injectable scaffold for bone repair). We noted that a static magnetic field could drive the FMSs to move to the desired site to form an FMS layer (Fig. 5a), mimicking the "chemotactic" effect of natural macrophages. It may realize the design that the FMSs moved to the target region to form an antibacterial layer after injection into the defect.

This FMS exhibits sensitive photothermal properties under NIR and
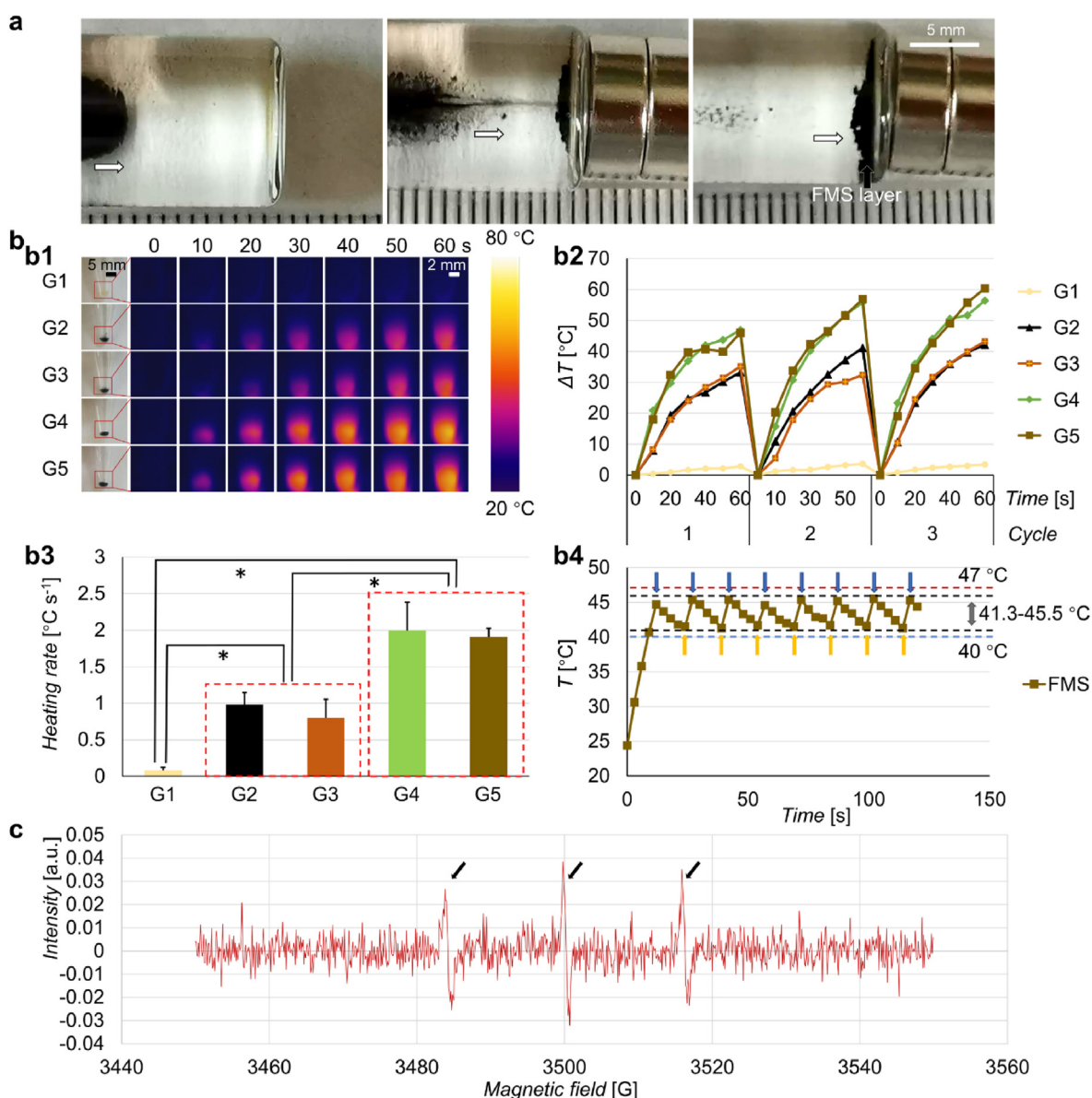
Fig. 5. FMS manipulated by the magnetic field and NIR. (a) The manipulation performance of FMS under magnetic field. FMSs in uncoagulated GelMA moved directionally to form an FMS layer under the static magnetic field. (b) The photothermal performance of FMSs under NIR. b1) Thermal image. b2) The heating curve, which showed a recyclable photothermal property. b3) The heating rate within 10 s of NIR irradiation. * indicates $P < 0.05$. b4) The temperature of FMSs was maintained at 41.3–45.5 °C by cyclically switching the power of NIR at 808 nm. Blue arrows refer to switching to 0.1 W cm^{-2}, and yellow arrows refer to switching to 0.5 W cm^{-2} (G1, pure GMS; G2, PDA-coated GMS; G3, PDA-coated GMS + MNP; G4, PDA-coated GMS + ANP; G5, PDA-coated GMS + MNP + ANP (i.e., FMS).) (c) The generation of ROS from FMSs by NIR. The generated ROS can be detected by EPR, which showed three characteristic peaks of $^1O_2$ (indicated by black arrows) in the obtained spectrum. (For interpretation of the references to colour in this figure legend, the reader is referred to the Web version of this article.)

can be heated cyclically (Fig. 5b1-2). We found that PDA-coated GMS and PDA-coated GMS + MNP have good photothermal properties, and the heating rate is significantly higher than that of GMS (Fig. 5b3), which mainly owed to the photothermal capacity of PDA [28,29]. As described in section 3.2.2, the ANP also had good photothermal properties. Therefore, the modification of ANP onto the PDA surface will result in the superimposition of the photothermal properties of PDA and ANP, leading to a more sensitive photothermal performance. Our experiment also verified this: compared with PDA-coated GMS and PDA-coated GMS + MNP, the heating rates for PDA-coated GMS + ANP and PDA-coated GMS + MNP + ANP (i.e., FMS) were further increased significantly (Fig. 5b3). In short, the sensitive photothermal performance of FMS was realized by the PDA coating and the ANPs. Based on the sensitive and cyclable photothermal properties of FMSs, we could stabilize the temperature of FMSs at 41.3–45.5 °C by cyclically switching the laser power

(two levels of 0.5 W cm^{-2} and 0.1 W cm^{-2}) (Fig. 5b4). This could not only melt the core of ANP and release IR780 to generate ROS for sterilization but also avoid damage to bone tissue (the maximum temperature tolerance of osteocytes is 47 °C [40]). Furthermore, the characteristics of cyclic heating may also bring the advantages of regular irradiation for regular sterilization in clinical applications.

The FMS can respond to NIR to generate ROS (photodynamic effect). $^1O_2$ is a type of ROS with a strong sterilization performance [17]. Three characteristic peaks of $^1O_2$ can be found in the EPR spectrum (Fig. 5c) with the radiation temperature at 41–45 °C, and the amount of $^1O_2$ was $2.20 \times 10^{12} \pm 4.32 \times 10^{11}$ spins mg^{-1}. This provides the possibility that the FMSs can generate ROS for sterilization within the tolerance temperature of osteogenesis-related cells [40], which ensures the feasibility of their antibacterial application in bone defect healing.
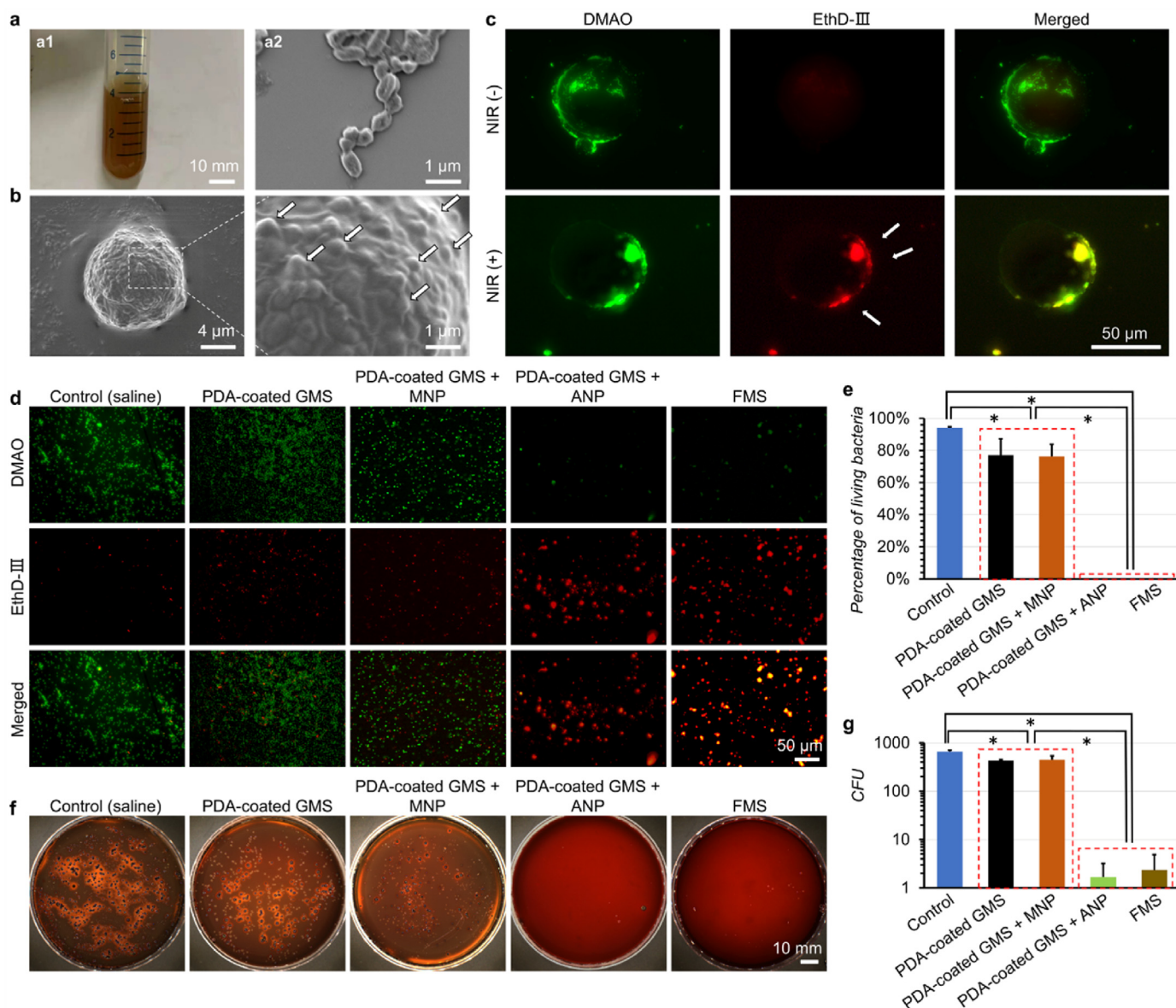
Fig. 6. Antibacterial properties of FMS *in vitro*. (a) Culture of the *P. gingivalis*. a1) Bacteria cultured in BHI liquid medium; a2) SEM image of bacteria. (b) SEM image of *P. gingivalis* on the surface of FMSs after co-culture for 24 h. White arrows indicate the *P. gingivalis*. (c) *P. gingivalis* on the surface of FMSs after co-culture for 24 h (live/dead bacterial staining). Green fluorescence represents all bacteria (live/dead), and red fluorescence represents dead bacteria. The white arrows indicate the *P. gingivalis* captured and killed on the surface of FMS. (d–e) Bacteria in the liquid medium after NIR irradiation (live/dead bacterial staining): (d) is the picture. green fluorescence represents all bacteria (live/dead), and red fluorescence represents dead bacteria, (e) is quantitative analysis. (f–g) CFU analysis of the *P. gingivalis* on BHI solid medium after culturing the NIR-irradiated material-bacterial mixtures for one week: (f) is the picture; (g) is the quantitative analysis. * indicates *P* < 0.05. (For interpretation of the references to colour in this figure legend, the reader is referred to the Web version of this article.)

3.4.2. Antibacterial properties of FMS in vitro

P. gingivalis is a common pathogen in oral infections. It is the primary pathogen for the occurrence and development of chronic periodontitis, which can lead to the resorption of alveolar bone [22]. We decided to explore the bactericidal ability of FMSs on *P. gingivalis* to evaluate the application possibility of FMS in the oral and maxillofacial regions. We cultured the *P. gingivalis* (Fig. 6a1), which possesses a rod-shaped morphology under SEM (Fig. 6a2), consistent with the normal cell morphology of *P. gingivalis* in previous studies [41–43].

We co-cultured FMSs with *P. gingivalis*. The SEM results showed that the FMSs trapped the bacteria on its surface (Fig. 6b), which may be realized by the catechol on the surface of the PDA coating [16]. The results of live and dead bacterial staining also verified the phenomenon of bacteria capture (the green fluorescence showed the location of bacteria under the inverted fluorescence microscope; Fig. 6c). No noticeable difference was found when comparing them with the PDA-coated GMS in the bacterial capture ability (Supplementary Information, Fig. S4). Furthermore, after NIR irradiation, FMSs killed bacteria on their surface (the red fluorescence showed the dead bacteria; Fig. 6c). This suggested that the FMS could capture and kill *P. gingivalis*, which is consistent with the bactericidal mechanism of natural macrophages [13,14].

Finally, we evaluated the antibacterial efficiency of the FMSs. After NIR irradiation, we found that the dead bacteria in the PDA-coated GMS group and the PDA-coated GMS + MNP group was slightly more than that of the normal saline group by live/dead bacterial staining (Fig. 6d). By

comparison, almost all bacteria were killed in the PDA-coated GMS + ANP group and the FMS group. The quantitative analysis results of this staining have a consistent trend: the percentage of viable bacteria in the PDA-coated GMS group and the PDA-coated GMS + MNP group was significantly lower than the control group, while the PDA-coated GMS + ANP group and the FMS group approached 0 and were significantly lower than the other three groups (Fig. 6e). The CFU analysis of *P. gingivalis* on BHI solid medium further verified the trend that only a small number of bacterial colonies were formed in the PDA-coated GMS + ANP group and the FMS group (Fig. 6f), significantly less than the saline group, the PDA-coated GMS group, and the PDA-coated GMS + MNP group (Fig. 6g). Summarizing the above phenomena, the groups containing PDA coating but without ANPs (the PDA-coated GMS group and the PDA-coated GMS + MNP group) possessed mild sterilizing performances. The reason may be that the heat produced by PDA-coating under the NIR irradiation destroyed the bacterial cell walls and membranes, leading to the leakage of cellular contents and, ultimately, bacterial death [35,44,45]. However, the working temperature in the study was controlled below 47 °C, which is lower than the conventional antibacterial photothermal therapy temperature [35,45], therefore only killing a small number of bacteria. Meanwhile, the groups where microspheres were further modified with ANPs (the PDA-coated GMS + ANP group and the FMS group) showed a sharp decline in viable bacteria, suggesting the dominant role of ANP in the antibacterial process. Furthermore, the antibacterial activity of ANP is mainly mediated by the heat and the ROS, while the temperatures were
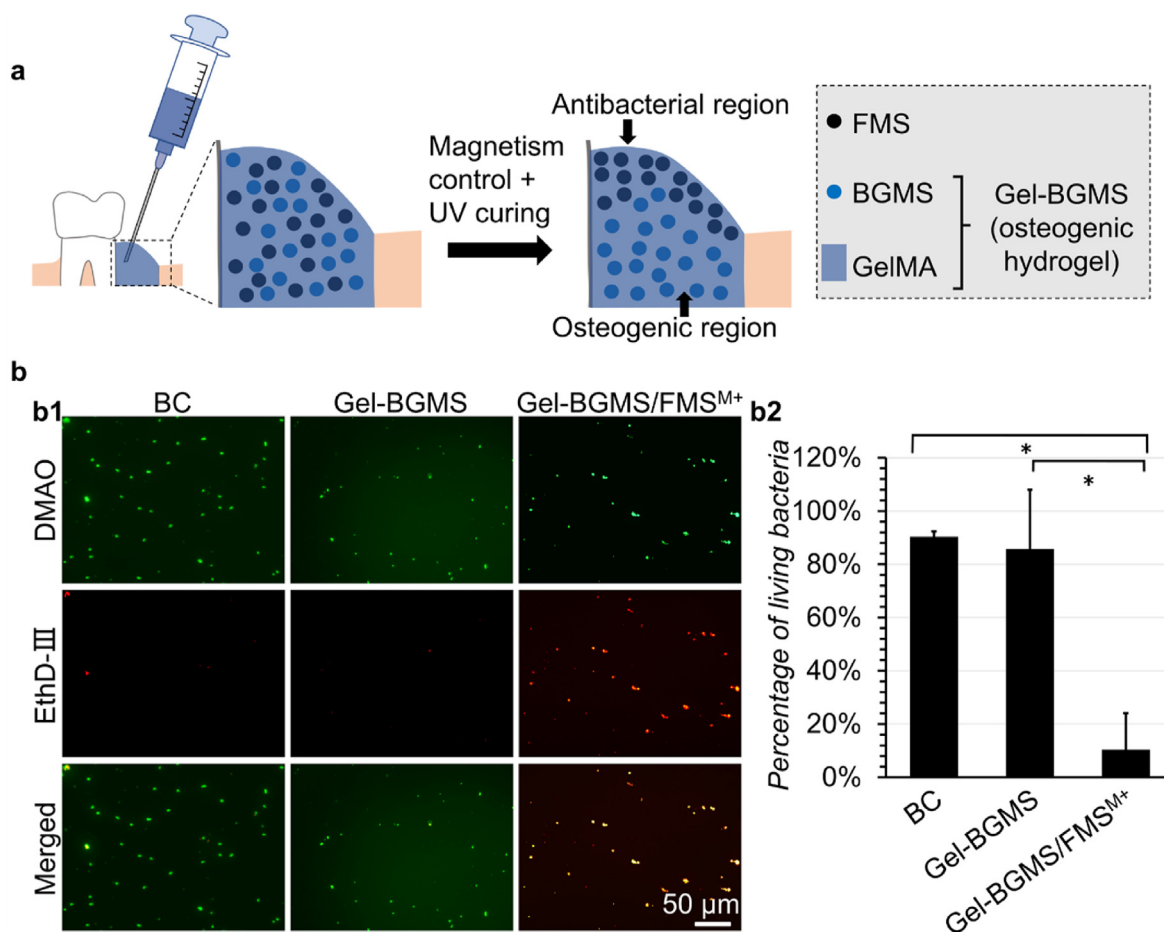

Fig. 7. The antibacterial application of FMSs in bone defects. (a) The schematic diagram. The FMSs were mixed with the uncured osteogenic hydrogel (Gel-BGMS), injected into the bone defect, driven by the magnetism to the desired region (such as the cervical surface of the tooth and the outer surface of the hydrogel system), and cured with UV. They established a defensive line to resist the attack from specific pathogens. (b) The live/dead bacterial staining of bacterial samples taken from the gingival sulcus and wound surface after the irradiation of NIR. b1) The photographs captured by the inverted fluorescence microscope. Green fluorescence represents all bacteria (live/dead), and red fluorescence represents dead bacteria. b2) The quantitative analysis of living bacterial percentage. * indicates $P < 0.05$. (For interpretation of the references to colour in this figure legend, the reader is referred to the Web version of this article.)

consistent (41–45 °C) in the above four groups. Therefore, mainly the ROS generated from the ANPs played a key bactericidal role. In short, all these results indicate that the FMS had a significant bactericidal effect on *P. gingivalis* even at a relatively lower temperature, which mainly owed to the ROS produced by the ANPs.

3.5. Application performances of FMS in vivo

For the excellent light-magnetism responsive and bactericidal

performances *in vitro*, the FMSs were further applied with injectable osteogenic hydrogel *in vivo* in this study. However, before the experiment *in vivo*, three points need to be made clear. The first is the selection of animal models. The inflammatory periodontal bone defect model induced by ligature placement, bacterial inoculation, and lipopolysaccharide local injection [46] can better mimic the occurrence and development of clinical periodontal disease, which is suitable for investigating pathogenesis. However, the size of bone defects varies among different individuals, making it difficult to accurately evaluate the antibacterial
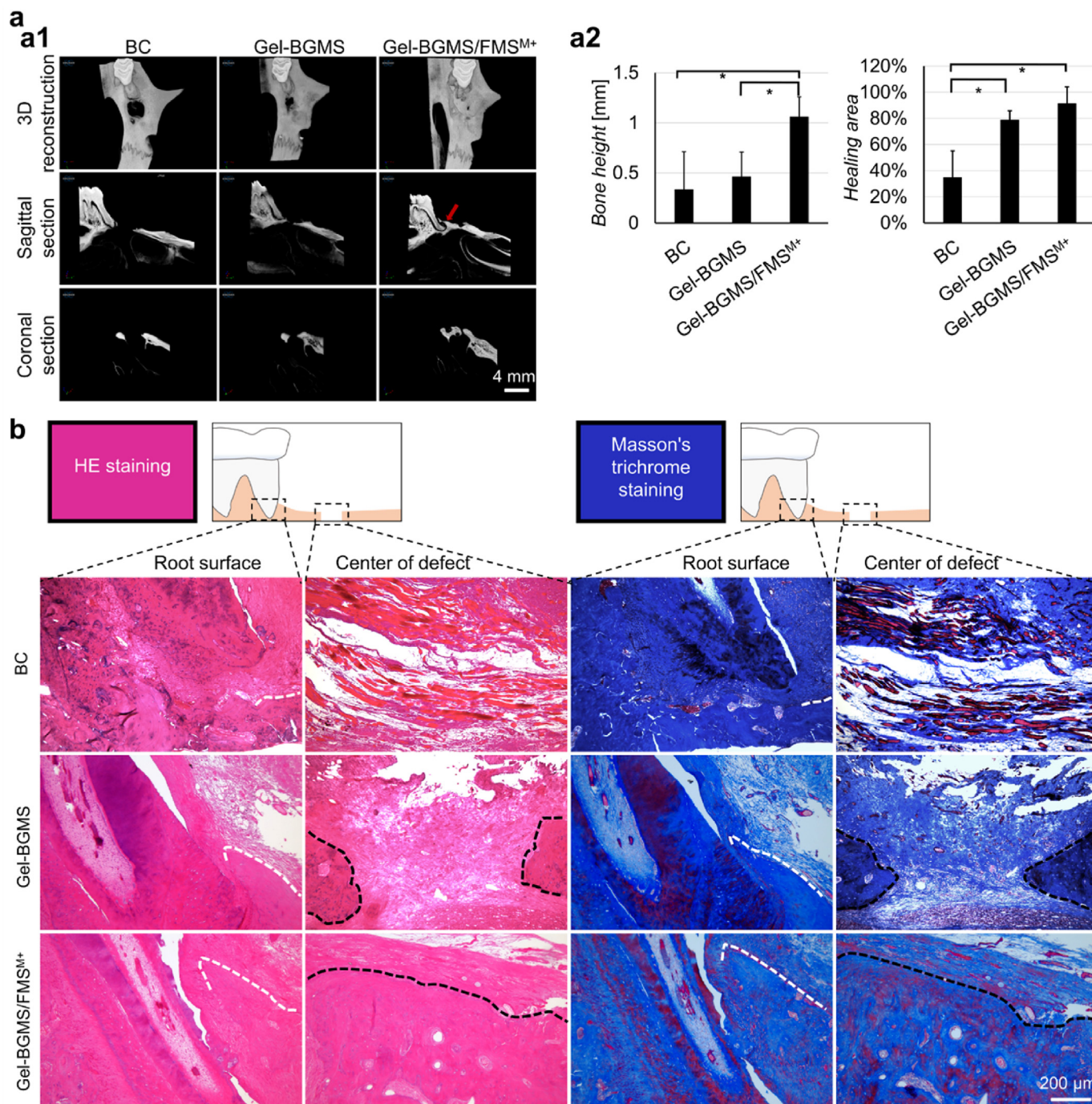
Fig. 8. The effects of FMSs on bone defect healing at 3 months post-surgery. (a) Micro-CT. a1) Images of 3D reconstruction and sectional view. The red arrow indicates the bone tissues regenerated on the mesial surface of the M1 mesial root. a2) The quantitative analyses of the regenerated bone height along the mesial surface of M1 and the bone healing area percentage. * indicates $P < 0.05$. (b) HE and Masson's trichrome-staining photographs showing the mesial surface of the M1 mesial root and the center of the bone defect. White lines show the bone tissues along the mesial root surfaces of M1, while black lines show the bone tissues in the defect center. (For interpretation of the references to colour in this figure legend, the reader is referred to the Web version of this article.)

and regenerative performances of the implanted materials. To address this issue, we combined trauma-induced bone defects with bacterial inoculation [47,48], ensuring defect size consistency among different individuals. The second is the dosage of BMP-2. In this study, BMP-2 was used as the active ingredient of the injectable osteogenic hydrogel (Gel-BGMS). It is a classic cytokine that promotes bone healing and is approved for clinical use by U.S. Food and Drug Administration in 2002 [49]. It should be noted that excessive BMP-2 will not promote bone regeneration and may instead cause inflammation and fat formation [2, 50,51]. The commonly used concentration of BMP-2 is 0.3–3 µg mL^{-1} [52,53]. In this study, the concentration of BMP-2 to soak GMSs was 100 µg mL^{-1}. The volume ratio between BMP-2 solution and the final hydrogel system was 3: 100, which means that the working concentration would not exceed the upper limit (3 µg mL^{-1}) even if all the loaded BMP-2 diffused rapidly, ensuring the safety of BMP-2 use. The third is the architecture implementation and biocompatibility of the hierarchical Gel-BGMS/FMS^{M+} system. Our design is as follows. Before curing with UV, the Gel-BGMS was mixed with FMSs and then injected into the bone defect adjacent to the M1. After the control by magnetism, the FMSs were distributed at the mesial neck of M1 and the outer surface of the gel system to resist attacks from specific pathogens in the gingival sulcus and wound surface (Fig. 7a). This strategy of attracting FMSs to the outer surface of the gel system by magnetism has been pre-implemented *in vitro* (Supplementary Information, Fig. S5), and the gel system with hierarchical structure at the microscale have been successfully realized (Supplementary Information, Fig. S6). Furthermore, *in vitro* experiments confirmed that heat and ROS produced by the antibacterial layer of the hierarchical system did not adversely affect the proliferation, penetration, osteogenic differentiation, and calcium salt deposition of bone marrow mesenchymal stem cells in the osteogenic region (Supplementary Information, Figs. S7–8), suggesting that it would have no detectable damage to the bone regeneration center if used *in vivo*. Therefore, the hierarchical Gel-BGMS/FMS^{M+} system was applied to the periodontal bone defect model in this study.

The live/dead bacterial staining results showed that the FMSs had a good antibacterial performance *in vivo* (Fig. 7b): they killed most *P. gingivalis* in the operative area (Fig. 7b1). The percentage of viable bacteria in the Gel-BGMS/FMS^{M+} group is 10.38 ± 13.68%, significantly lower than the BC group (90.34 ± 2.01%) and Gel-BGMS group (85.69 ± 22.29%) (Fig. 7b2).

Since *P. gingivalis* can result in bone absorption by secreting proteases and endotoxins [54,55], killing *P. gingivalis* by FMSs may offset their bone absorption effect to promote bone defect healing. Further experiments confirmed this hypothesis. The results of micro-CT (Fig. 8a) suggested that the Gel-BGMS/FMS^{M+} group had a significantly higher bone height on the M1 mesial surface compared with the other groups. Furthermore, the Gel-BGMS/FMS^{M+} group had a better bone healing performance from the results of 3D reconstruction, although there is no significant difference in the quantitative analysis of the bone healing area compared to the Gel-BGMS group. The better bone healing performance may also be caused by the mild localized heat generated by FMSs under NIR, which can promote osteogenic differentiation of osteogenesis-related cells by activating the BMP pathway [56,57]. The results of HE and Masson's trichrome-staining further verified the tendency that the Gel-BGMS/FMS^{M+} group had a higher bone height along root surfaces and a better bone healing performance (Fig. 8b). In short, the FMS can kill specific pathogens (such as *P. gingivalis*) in a predetermined region in the organism with the control by magnetism and NIR, thus inhibiting bone resorption along root surface and promoting bone defect healing. Finally, we also tested the visceral toxicity of FMSs in the hierarchical system. No sign of organ damage can be observed in the histological structure of heart, liver, spleen, lung and kidney, and no noticeable difference was found when comparing Gel-BGMS/FMS^{M+} group with Gel-BGMS group and BC group (Supplementary Information, Fig. S9). It suggested that the FMS had no obvious visceral toxicity in this application, further proving its good biocompatibility.

The hierarchical gel system constructed with FMSs has achieved good performances *in vivo*. In fact, injecting the Gel-BGMS system and microspheres modified with ANPs step by step may also realize the hierarchical gel system. However, the magnetic design strategy used in our study has three advantages: 1, it can be administered in one step, simplifying the operating procedures; 2, the composition ratio of the gel system to FMSs was constant; 3, if the infection is in a deep region, we can also conveniently move FMSs to the infection site by magnetism.

In addition, the good NIR controllability and antibacterial property of FMS also played an important role. Although a series of photo-responsive antibacterial materials have been previously reported [35,44,45], the FMS has its uniqueness in usage as additives for bone regeneration materials, which means the demand for a milder working temperature (the maximum temperature tolerance of osteocytes is 47 °C [40]). Based on the sensitive photothermal performance of FMS, we controlled the temperature below 47 °C by cyclic switching the power. The FMSs still showed excellent antibacterial performances at such lower temperatures, avoiding the damage to osteocytes caused by excessive temperature and guaranteeing the healing effect of bone defects. The FMS constructed in this study provides an effective way to satisfy the antibacterial demands after periodontal surgery. It can be used as the additive of injectable osteogenic hydrogel to precisely inhibit the colonization of *P. gingivalis* and guarantee the healing of periodontal bone defects, possessing a clinical application prospect in treating periodontal disease. The application range of FMS is expected to be further expanded in the future. Appropriate anatomical structures, such as the digestive tract or joint cavity, may be more conducive to the function of FMS.

4. Conclusion

In this study, we constructed the magnetic microsphere that mimics certain macrophage functions by integrating IR780, magnetism, and PDA into a microsphere in an organized way. It possessed a rough surface and could mimic the directional movement, capture, and bactericidal function like natural macrophages under the manipulation of magnetic fields and NIR light. Furthermore, the functionalized microspheres can be combined with injectable osteogenic materials *in vivo* and be driven to the target region for sterilization, protecting the healing environment of bone defects. This gave us a promising strategy to construct an intelligent, responsive antibacterial material to meet the precise antibacterial demand during bone defect healing.

Credit author statement

Qiao Zhou: Investigation, Formal analysis, Writing – Original Draft. **Jun Liu:** Conceptualization, Methodology, Writing – Review & Editing. **Jia Yan and Zhaobin Guo:** Investigation, Validation, Writing – Review & Editing. **Feimin Zhang:** Conceptualization, Supervision, Funding acquisition, Resources.

Declaration of competing interest

The authors declare that they have no known competing financial interests or personal relationships that could have appeared to influence the work reported in this paper.

Data availability

Data will be made available on request.

Acknowledgments

Program Development of Jiangsu Higher Education Institutions (PAPD, 2018–87).

Appendix A. Supplementary data

Supplementary data to this article can be found online at https://doi.org/10.1016/j.mtbio.2023.100651.

References

[1] J.G. Wijbenga, R.H. Schepers, P.M.N. Werker, M.J.H. Witjes, P.U. Dijkstra, A systematic review of functional outcome and quality of life following reconstruction of maxillofacial defects using vascularized free fibula flaps and dental rehabilitation reveals poor data quality, J. Plast. Reconstr. Aesthetic Surg. 69 (8) (2016) 1024–1036, https://doi.org/10.1016/j.bjps.2016.05.003.

[2] J. Tan, M. Zhang, Z. Hai, C. Wu, J. Lin, W. Kuang, H. Tang, Y. Huang, X. Chen, G. Liang, Sustained release of two bioactive factors from supramolecular hydrogel promotes periodontal bone regeneration, ACS Nano 13 (5) (2019) 5616–5622, https://doi.org/10.1021/acsnano.9b00788.

[3] S. Sowmya, U. Mony, P. Jayachandran, S. Reshma, R.A. Kumar, H. Arzate, S.V. Nair, R. Jayakumar, Tri-layered nanocomposite hydrogel scaffold for the concurrent regeneration of cementum, periodontal ligament, and alveolar bone, Adv. Healthcare Mater. 6 (7) (2017), 1601251, https://doi.org/10.1002/adhm.201601251.

[4] S. Kitamura, Anatomy of the fasciae and fascial spaces of the maxillofacial and the anterior neck regions, Anat. Sci. Int. 93 (1) (2018) 1–13, https://doi.org/10.1007/s12565-017-0394-x.

[5] L. Xu, Q. Ye, J. Xie, J. Yang, W. Jiang, H. Yuan, J. Li, An injectable gellan gum-based hydrogel that inhibits Staphylococcus aureus for infected bone defect repair, J. Mater. Chem. B 10 (2) (2022) 282–292, https://doi.org/10.1039/D1TB02230J.

[6] A. Meinen, A. Reuss, N. Willrich, M. Feig, I. Noll, T. Eckmanns, B. Al-Nawas, R. Markwart, Antimicrobial resistance and the spectrum of pathogens in dental and oral-maxillofacial infections in hospitals and dental practices in Germany, Front. Microbiol. 12 (2021), 676108, https://doi.org/10.3389/fmicb.2021.676108.

[7] S. Kondoh, K. Matsuo, S. Yuzuriha, N. Kikuchi, R. Ban, Dressing for alveolopalatal wounds after alveolar bone grafting, Ann. Plast. Surg. 51 (3) (2003) 290–293, https://doi.org/10.1097/01.SAP.0000063757.61972.54.

[8] T. Cai, L. Zhang, K. Zhu, J. Hu, T. Zhan, L. Liu, C. Li, C. Zhang, Retrospective clinical evaluation of negative-pressure wound therapy for infection prevention following malignant pelvic bone tumor resection reconstruction, Adv. Skin Wound Care 34 (1) (2021) 1–6, https://doi.org/10.1097/01.ASW.0000723280.71047.73.

[9] C. Cao, N. Yang, Y. Zhao, D. Yang, Y. Hu, D. Yang, X. Song, W. Wang, X. Dong, Biodegradable hydrogel with thermo-response and hemostatic effect for photothermal enhanced anti-infective therapy, Nano Today 39 (2021), 101165, https://doi.org/10.1016/j.nantod.2021.101165.

[10] S.B. Levy, B. Marshall, Antibacterial resistance worldwide: causes, challenges and responses, Nat. Med. 10 (12) (2004) S122–S129, https://doi.org/10.1038/nm1145.

[11] J.L. Mège, V. Mehraj, C. Capo, Macrophage polarization and bacterial infections, Curr. Opin. Infect. Dis. 24 (3) (2011) 230–234, https://doi.org/10.1097/QCO.0b013e328344b73e.

[12] A. Sica, P. Larghi, A. Mancino, L. Rubino, C. Porta, M.G. Totaro, M. Rimoldi, S.K. Biswas, P. Allavena, A. Mantovani, Macrophage polarization in tumour progression, Semin. Cancer Biol. 18 (5) (2008) 349–355, https://doi.org/10.1016/j.semcancer.2008.03.004.

[13] J.D. Thiriot, Y.B. Martinez-Martinez, J.J. Endsley, A.G. Torres, Hacking the host: exploitation of macrophage polarization by intracellular bacterial pathogens, Pathog. Dis. 78 (1) (2020), https://doi.org/10.1093/femspd/ftaa009 ftaa009.

[14] L. Gong, R.J. Devenish, M. Prescott, Autophagy as a macrophage response to bacterial infection, IUBMB Life 64 (9) (2012) 740–747, https://doi.org/10.1002/iub.1070.

[15] Q.Q. Lei, Y.W. Zhang, W.N. Zhang, R.W. Li, N.J. Ao, H. Zhang, A synergy between dopamine and electrostatically bound bactericide in a poly (vinyl alcohol) hybrid hydrogel for treating infected wounds, Carbohydr. Polym. 272 (15) (2021), 118513, https://doi.org/10.1016/j.carbpol.2021.118513.

[16] D. Gan, T. Xu, W. Xing, X. Ge, L. Fang, K. Wang, F. Ren, X. Lu, Mussel-inspired contact-active antibacterial hydrogel with high cell affinity, toughness, and recoverability, Adv. Funct. Mater. 29 (1) (2019), 1805964, https://doi.org/10.1002/adfm.201805964.

[17] L. Tan, J. Li, X.M. Liu, Z.D. Cui, X.J. Yang, S.L. Zhu, Z.Y. Li, X.B. Yuan, Y.F. Zheng, K.W.K. Yeung, H.B. Pan, X.B. Wang, S.L. Wu, Rapid biofilm eradication on bone implants using red phosphorus and near-infrared light, Adv. Mater. 30 (31) (2018), 1801808, https://doi.org/10.1002/adma.201801808.

[18] S.S. Ren, Y. Zhou, R.Y. Fan, W.Z. Peng, X.W. Xu, L. Li, Y. Xu, Constructing biocompatible MSN@Ce@PEG nanoplatform for enhancing regenerative capability of stem cell via ROS-scavenging in periodontitis, Chem. Eng. J. 423 (2021), 130207, https://doi.org/10.1016/j.cej.2021.130207.

[19] G. Go, J. Han, J. Zhen, S. Zheng, A. Yoo, M.-J. Jeon, J.-O. Park, S. Park, A magnetically actuated microscaffold containing mesenchymal stem cells for articular cartilage repair, Adv. Healthcare Mater. 6 (13) (2017), 1601378, https://doi.org/10.1002/adhm.201601378.

[20] C. Zhu, D. Huo, Q. Chen, J. Xue, S. Shen, Y. Xia, A eutectic mixture of natural fatty acids can serve as the gating material for near-infrared-triggered drug release, Adv. Mater. 29 (40) (2017), 1703702, https://doi.org/10.1002/adma.201703702.

[21] H. Lee, J. Rho, P.B. Messersmith, Facile conjugation of biomolecules onto surfaces via mussel adhesive protein inspired coatings, Adv. Mater. 21 (4) (2009) 431–434, https://doi.org/10.1002/adma.200801222.

[22] A. Lo, C. Seers, S. Dashper, C. Butler, G. Walker, K. Walsh, D. Catmull, B. Hoffmann, S. Cleal, P. Lissel, J. Boyce, E. Reynolds, FimR and FimS: biofilm formation and gene expression in Porphyromonas gingivalis, J. Bacteriol. 192 (5) (2010) 1332–1343, https://doi.org/10.1128/JB.01211-09.

[23] B. Sulijaya, M. Yamada-Hara, M. Yokoji-Takeuchi, Y. Matsuda-Matsukawa, K. Yamazaki, A. Matsugishi, T. Tsuzuno, K. Sato, Y. Aoki-Nonaka, N. Takahashi, S. Kishino, J. Ogawa, K. Tabeta, K. Yamazaki, Antimicrobial function of the polyunsaturated fatty acid KetoC in an experimental model of periodontitis, J. Periodontol. 90 (12) (2019) 1470–1480, https://doi.org/10.1002/JPER.19-0130.

[24] D. Yang, X. Lv, L. Xue, N. Yang, Y. Hu, L. Weng, N. Fu, L. Wang, X. Dong, A lipase-responsive antifungal nanoplatform for synergistic photodynamic/photothermal/pharmaco-therapy of azole-resistant Candida albicans infections, Chem. Commun. 55 (100) (2019) 15145–15148, https://doi.org/10.1039/C9CC08463K.

[25] F. Krombach, S. Münzing, A.M. Allmeling, J.T. Gerlach, J. Behr, M. Dörger, Cell size of alveolar macrophages: an interspecies comparison, Environ. Health Perspect. 105 (Suppl 5) (1997) 1261–1263, https://doi.org/10.1289/ehp.97105s51261. Suppl 5.

[26] E. Faure, C. Falentin-Daudre, C. Jerome, J. Lyskawa, D. Fournier, P. Woisel, C. Detrembleur, Catechols as versatile platforms in polymer chemistry, Prog. Polym. Sci. 38 (1) (2013) 236–270, https://doi.org/10.1016/j.progpolymsci.2012.06.004.

[27] W. Cheng, X. Zeng, H. Chen, Z. Li, W. Zeng, L. Mei, Y. Zhao, Versatile polydopamine platforms: synthesis and promising applications for surface modification and advanced nanomedicine, ACS Nano 13 (8) (2019) 8537–8565, https://doi.org/10.1021/acsnano.9b04436.

[28] M. Li, X. Sun, N. Zhang, W. Wang, Y. Yang, H. Jia, W. Liu, NIR-activated polydopamine-coated carrier-free "nanobomb" for in situ on-demand drug release, Adv. Sci. 5 (7) (2018), 1800155, https://doi.org/10.1002/advs.201800155.

[29] H. Wang, Y. Jin, Y. Tan, H. Zhu, W. Huo, P. Niu, Z. Li, J. Zhang, X.-j. Liang, X. Yang, Photo-responsive hydrogel facilitates nutrition deprivation by an ambidextrous approach for preventing cancer recurrence and metastasis, Biomaterials 275 (2021), 120992, https://doi.org/10.1016/j.biomaterials.2021.120992.

[30] P.J. Moncure, Z.C. Simon, J.E. Millstone, Relationship between gel mesh and particle size in determining nanoparticle diffusion in hydrogel nanocomposites, J. Phys. Chem. B 126 (22) (2022) 4132–4142, https://doi.org/10.1021/acs.jpcb.2c00771.

[31] J. Thevenot, A.-L. Troutier, L. David, T. Delair, C. Ladavière, Steric stabilization of lipid/polymer particle assemblies by poly(ethylene glycol)-lipids, Biomacromolecules 8 (11) (2007) 3651–3660, https://doi.org/10.1021/bm700753q.

[32] C. Zhang, T. Liu, Y. Su, S. Luo, Y. Zhu, X. Tan, S. Fan, L. Zhang, Y. Zhou, T. Cheng, C. Shi, A near-infrared fluorescent heptamethine indocyanine dye with preferential tumor accumulation for in vivo imaging, Biomaterials 31 (25) (2010) 6612–6617, https://doi.org/10.1016/j.biomaterials.2010.05.007.

[33] L. Yan, H. Wang, A. Zhang, C. Zhao, Y. Chen, X. Li, Bright and stable near-infrared Pluronic–silica nanoparticles as contrast agents for in vivo optical imaging, J. Mater. Chem. B 4 (33) (2016) 5560–5566, https://doi.org/10.1039/C6TB01234E.

[34] K. Wang, Y. Zhang, J. Wang, A. Yuan, M. Sun, J. Wu, Y. Hu, Self-assembled IR780-loaded transferrin nanoparticles as an imaging, targeting and PDT/PTT agent for cancer therapy, Sci. Rep. 6 (1) (2016), 27421, https://doi.org/10.1038/srep27421.

[35] X. Qi, Y. Xiang, E. Cai, S. You, T. Gao, Y. Lan, H. Deng, Z. Li, R. Hu, J. Shen, All-in-one: harnessing multifunctional injectable natural hydrogels for ordered therapy of bacteria-infected diabetic wounds, Chem. Eng. J. 439 (2022), 135691, https://doi.org/10.1016/j.cej.2022.135691.

[36] M. Chen, H. Tan, W. Xu, Z. Wang, J. Zhang, S. Li, T. Zhou, J. li, X. Niu, A self-healing, magnetic and injectable biopolymer hydrogel generated by dual cross-linking for drug delivery and bone repair, Acta Biomater. 153 (2022) 159–177, https://doi.org/10.1016/j.actbio.2022.09.036.

[37] Y. Yang, X. Wu, L. Ma, C. He, S. Cao, Y. Long, J. Huang, R.D. Rodriguez, C. Cheng, C. Zhao, L. Qiu, Bioinspired spiky peroxidase-mimics for localized bacterial capture and synergistic catalytic sterilization, Adv. Mater. 33 (8) (2021), 2005477, https://doi.org/10.1002/adma.202005477.

[38] Y.-Q. Li, B. Zhu, Y. Li, W.R. Leow, R. Goh, B. Ma, E. Fong, M. Tang, X. Chen, A synergistic capture strategy for enhanced detection and elimination of bacteria, Angew. Chem., Int. Ed. 53 (23) (2014) 5837–5841, https://doi.org/10.1002/anie.201310135.

[39] R. Singh, V. Dubey, D. Wolfson, A. Ahmad, A. Butola, G. Acharya, D.S. Mehta, P. Basnet, B.S. Ahluwalia, Quantitative assessment of morphology and sub-cellular changes in macrophages and trophoblasts during inflammation, Biomed. Opt Express 11 (7) (2020) 3733–3752, https://doi.org/10.1364/BOE.389350.

[40] R.A. Eriksson, T. Albrektsson, The effect of heat on bone regeneration: an experimental study in the rabbit using the bone growth chamber, J. Oral Maxillofac. Surg. 42 (11) (1984) 705–711, https://doi.org/10.1016/0278-2391(84)90417-8.

[41] L. Xu, X. Yu, W. Chen, S. Zhang, J. Qiu, Biocorrosion of pure and SLA titanium surfaces in the presence of Porphyromonas gingivalis and its effects on osteoblast behavior, RSC Adv. 10 (14) (2020) 8198–8206, https://doi.org/10.1039/D0RA00154F.

[42] A. El-Awady, M. de Sousa Rabelo, M.M. Meghil, M. Rajendran, M. Elashiry, A.F. Stadler, A.M. Foz, C. Susin, G.A. Romito, R.M. Arce, C.W. Cutler, Polymicrobial synergy within oral biofilm promotes invasion of dendritic cells and survival of consortia members, Biofilms 5 (1) (2019) 11, https://doi.org/10.1038/s41522-019-0084-7.

[43] K. Mukaddam, M. Astasov-Frauenhoffer, E. Fasler-Kan, L. Marot, M. Kisiel, E. Meyer, J. Köser, M. Waser, M.M. Bornstein, S. Kühl, Effect of a nanostructured titanium surface on gingival cell adhesion, viability and properties against p. gingivalis, Materials 14 (24) (2021) 7686, https://doi.org/10.3390/ma14247686.

[44] Z. Li, S. You, R. Mao, Y. Xiang, E. Cai, H. Deng, J. Shen, X. Qi, Architecting polyelectrolyte hydrogels with Cu-assisted polydopamine nanoparticles for photothermal antibacterial therapy, Mater, Today Bio 15 (2022), 100264, https://doi.org/10.1016/j.mtbio.2022.100264.

[45] Y. Xiang, X. Qi, E. Cai, C. Zhang, J. Wang, Y. Lan, H. Deng, J. Shen, R. Hu, Highly efficient bacteria-infected diabetic wound healing employing a melanin-reinforced biopolymer hydrogel, Chem. Eng. J. 460 (2023), 141852, https://doi.org/10.1016/j.cej.2023.141852.

[46] R.S. de Molon, C.H. Park, Q. Jin, J. Sugai, J.A. Cirelli, Characterization of ligature-induced experimental periodontitis, Microsc. Res. Tech. 81 (12) (2018) 1412–1421, https://doi.org/10.1002/jemt.23101.

[47] A.Y. Baştuğ, C.Ö. Tomruk, E. Güzel, İ. Özdemir, G. Duygu, E. Kütan, G.M.Y. Ülker, F.Ö. Arıcı, The effect of local application of thymoquinone, Nigella sativa's bioactive component, on bone healing in experimental bone defects infected with Porphyromonas gingivalis, J. Periodontal Implant Sci. 52 (3) (2022) 206–219.

[48] J.A. Ferreira, K.Z. Kantorski, N. Dubey, A. Daghrery, J.C. Fenno, Y. Mishina, H.-L. Chan, G. Mendonça, M.C. Bottino, Personalized and defect-specific antibiotic-laden scaffolds for periodontal infection ablation, ACS Appl. Mater. Interfaces 13 (42) (2021) 49642–49657, https://doi.org/10.1021/acsami.1c11787.

[49] E. Migliorini, A. Valat, C. Picart, E.A. Cavalcanti-Adam, Tuning cellular responses to BMP-2 with material surfaces, Cytokine Growth Factor Rev. 27 (2016) 43–54, https://doi.org/10.1016/j.cytogfr.2015.11.008.

[50] H. Tian, J. Du, J. Wen, Y. Liu, S.R. Montgomery, T.P. Scott, B. Aghdasi, C. Xiong, A. Suzuki, T. Hayashi, M. Ruangchainikom, K. Phan, G. Weintraub, A. Raed, S.S. Murray, M.D. Daubs, X. Yang, X.-b. Yuan, J.C. Wang, Y. Lu, Growth-Factor nanocapsules that enable tunable controlled release for bone regeneration, ACS Nano 10 (8) (2016) 7362–7369, https://doi.org/10.1021/acsnano.5b07950.

[51] L. Krishnan, L.B. Priddy, C. Esancy, B.S. Klosterhoff, H.Y. Stevens, L. Tran, R.E. Guldberg, Delivery vehicle effects on bone regeneration and heterotopic ossification induced by high dose BMP-2, Acta Biomater. 49 (2017) 101–112, https://doi.org/10.1016/j.actbio.2016.12.012.

[52] L.B. Priddy, O. Chaudhuri, H.Y. Stevens, L. Krishnan, B.A. Uhrig, N.J. Willett, R.E. Guldberg, Oxidized alginate hydrogels for bone morphogenetic protein-2 delivery in long bone defects, Acta Biomater. 10 (10) (2014) 4390–4399, https://doi.org/10.1016/j.actbio.2014.06.015.

[53] J. Ratanavaraporn, H. Furuya, H. Kohara, Y. Tabata, Synergistic effects of the dual release of stromal cell-derived factor-1 and bone morphogenetic protein-2 from hydrogels on bone regeneration, Biomaterials 32 (11) (2011) 2797–2811, https://doi.org/10.1016/j.biomaterials.2010.12.052.

[54] M. Kuboniwa, J.R. Houser, E.L. Hendrickson, Q. Wang, S.A. Alghamdi, A. Sakanaka, D.P. Miller, J.A. Hutcherson, T. Wang, D.A.C. Beck, M. Whiteley, A. Amano, H. Wang, E.M. Marcotte, M. Hackett, R.J. Lamont, Metabolic crosstalk regulates Porphyromonas gingivalis colonization and virulence during oral polymicrobial infection, Nat. Microbiol. 2 (11) (2017) 1493–1499, https://doi.org/10.1038/s41564-017-0021-6.

[55] W. Xu, W. Zhou, H. Wang, S. Liang, Chapter Two - Roles of Porphyromonas gingivalis and its virulence factors in periodontitis, in: R. Donev (Ed.), Adv. Protein Chem. Struct. Biol., Academic Press2020, pp. 45-84. https://doi.org/https://doi.org/10.1016/bs.apcsb.2019.12.001.

[56] Z. Zhang, Y. Ma, S. Guo, Y. He, G. Bai, W. Zhang, Low-intensity pulsed ultrasound stimulation facilitates in vitro osteogenic differentiation of human adipose-derived stem cells via up-regulation of heat shock protein (HSP)70, HSP90, and bone morphogenetic protein (BMP) signaling pathway, Biosci. Rep. 38 (3) (2018), BSR20180087, https://doi.org/10.1042/BSR20180087.

[57] X. Zhang, G. Cheng, X. Xing, J. Liu, Y. Cheng, T. Ye, Q. Wang, X. Xiao, Z. Li, H. Deng, Near-infrared light-triggered porous AuPd alloy nanoparticles to produce mild localized heat to accelerate bone regeneration, J. Phys. Chem. Lett. 10 (15) (2019) 4185–4191, https://doi.org/10.1021/acs.jpclett.9b01735.